CERN – EUROPEAN ORGANIZATION FOR NUCLEAR RESEARCH

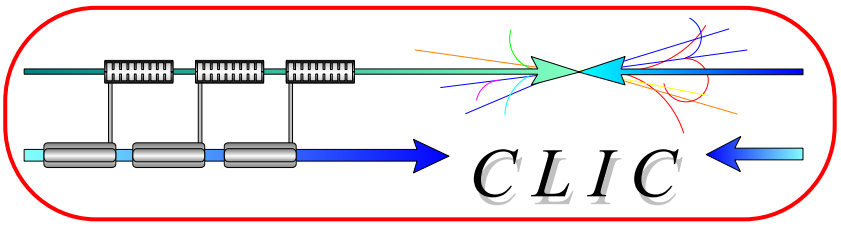

CLIC Note 551

CERN-OPEN-2003-008
27 January 2003

CLIC BEAM DELIVERY SYSTEM

M. Aleksa, R. Assmann, H. Burkhardt, J.-B. Jeanneret, S. Redaelli, T. Risselada,
S. Russenschuck, D. Schulte, F. Zimmermann, CERN, Geneva, Switzerland;
A. Faus-Golfe, IFIC, Valencia, Spain;
G.A. Blair, Royal Holloway, London, UK

Abstract

We review the present design for the CLIC beam delivery system as configured for 3 TeV and for 500 GeV, describe some recent developments (including the combined effect of solenoid, crab cavity, and crossing angle), highlight open questions, and outline future studies.

Presented at the 26th Advanced ICFA Beam Dynamics Workshop on Nanometre-Size Colliding Beams (Nanobeam2002), Lausanne, September 2-6, 2002

Geneva, Switzerland
24/01/2003

CLIC Beam Delivery System

M. Aleksa, R. Assmann, H. Burkhardt, J.-B. Jeanneret, S. Redaelli, T. Risselada, S. Russenschuck, D. Schulte, F. Zimmermann, CERN, Geneva, Switzerland; A. Faus-Golfe, IFIC, Valencia, Spain; G.A. Blair, Royal Holloway, London, UK

Abstract

We review the present design for the CLIC beam delivery system as configured for 3 TeV and for 500 GeV, describe some recent developments (including the combined effect of solenoid, crab cavity, and crossing angle), highlight open questions, and outline future studies.

1 INTRODUCTION

The CLIC beam-delivery system (BDS) comprises energy collimation, betatron collimation, final focus, interaction region, and the exit line for the spent beam. In this report, we describe the present BDS designs for centre-of-mass energies of 3 TeV and 500 GeV. The final focus was previously presented in Refs. [1, 2], and the collimation system in Refs. [2, 3].

The report is organized as follows. In Section 2 we discuss the parameters and the overall layout. Section 3 describes the optics for collimation system and final focus, and the simulated luminosity performance. Section 4 addresses the Interaction Region (IR). Section 5 discusses collimation issues. An alternative nonlinear collimation optics is presented in Section 6. Section 7 looks at the exit line. Section 8 summarizes the spin transport. Conclusions are drawn in Section 9.

2 PARAMETERS AND LAYOUT

Table 1 lists the design optics and beam parameters for the CLIC beam delivery system at two different energies. The values for 3 TeV listed in parentheses refer to an earlier much longer final-focus [4] and collimation system. They were added to the table to illustrate the progress made over the last two years: the total length per side of the interaction point was shortened from an initial value of 8.9 km to 2.5 km, by replacing the conventional final focus with a new compact design [5], omitting half of the energy collimation and further shortening the remainder. At the same time, the free length between the last quadrupole and the interaction point (IP) was more than doubled in the new compact final focus, and the vertical IP beta function was reduced by about a factor of two. Minimal changes were made to the 3-TeV design, in order to arrive at the 500-GeV system. The total length was kept the same. The emittances quoted in the table refer to the entrance of the beam delivery system.

The luminosity numbers quoted were obtained by MAD tracking, and include neither pinch nor hourglass effect. The luminosity enhancement due to the pinch effect is about a factor 2.2, so that the expected total luminosity at 3 TeV is close to 10^{35} cm^{-2}s^{-1}. At 500 GeV, the luminosity is about half this value, assuming a two times increased repetition rate of 200 Hz. The initial momentum distribution used in the multi-particle tracking was obtained by a CLIC linac simulation with the PLACET code, and represents the combined effects of multi-bunch beam loading, short-range wake fields, rf curvature, and rf phase (BNS damping).

Table 1: Final-focus (FF), collimation system (CS), and beam parameters at 3 TeV and 500 GeV cm energy. Emittance numbers refer to the entrance of the BDS. Shown in parentheses are earlier values [1, 3, 4], illustrating the evolution of the design. The spot sizes quoted refer to the rms values obtained by particle tracking and are larger than the 'effective' beam sizes which determine the luminosity.

parameter	symbol	3 TeV	500 GeV
FF length [km]		0.5 (3.1)	0.5
CS length [km]		2.0 (5.8)	2.0
BDS length [km]		2.5 (8.9)	2.5
hor. emittance [μm]	$\gamma\epsilon_x$	0.68	2.0
vert. emittance [nm]	$\gamma\epsilon_y$	10 (20)	10
hor. beta function [mm]	β_x^*	6.0 (8.0)	3.0
vert. beta function [mm]	β_y^*	0.07 (0.15)	0.05
rms spot size [nm]	$\sigma_{x,y}^*$	67, 2.1	180, 4.2
bunch length [μm]	σ_z^*	35 (30)	35
IP free length	l^*	4.3 (2.0)	4.3
crossing angle [mrad]	θ_c	20	20
repetition rate [Hz]	$f_{\rm rep}$	100	200
lum. w/o pinch [10^{34} cm^{-2}s^{-1}]	L_0	4.0	1.9

3 OPTICS AND PERFORMANCE

3.1 3-TeV Design

Figure 1 shows a previous optics design for the CLIC beam delivery system presented at PAC2001 [3], which consists of a Raimondi final focus à la NLC [5], and a long collimation system derived from Ref. [6]. The length of the energy collimation section has been scaled by a factor 8 and its bending angles by a factor 1/32 with respect to the 1 TeV NLC design [6]. The IP beta functions are $\beta_x^* = 8$ mm, $\beta_y^* = 150$ μm; the free length from the IP is $l^* = 4.3$ m;

and the estimated horizontal emittance growth from synchrotron radiation is

$$\Delta(\gamma\epsilon_x) \approx (4\times10^{-8}\ \mathrm{m^2/GeV^{-6}})E^6 I_5 \approx 9\ \mathrm{nm}\ , \quad (1)$$

where the radiation integral

$$I_5 = \int \frac{\mathcal{H}}{|\rho|^3}\, ds \quad (2)$$

is $I_5 \approx 1.8\times10^{-20}$ m ($\mathcal{H} = (1/\beta)(D^2+(\beta D' - \frac{1}{2}\beta' D)^2)$). Note that most of the collimation length, about 5 km, is dedicated to the collimation of off-momentum particles.

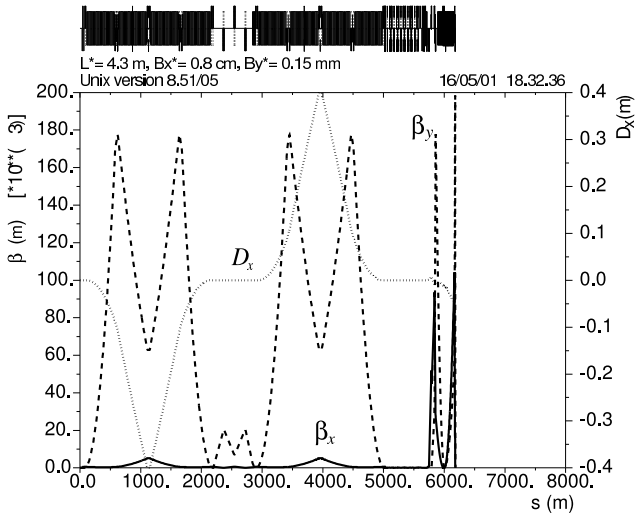

Figure 1: Optics of 3-TeV beam delivery system with long collimation section, as of June 2001.

Figure 2 displays the present optics. The collimation system was shortened compared with Fig. 1, by rescaling the length of the energy collimation section (by a factor 0.625), while increasing the bending angles θ_b (by a factor $\times 2.67$); and omitting half of the energy collimation altogether. The compact final focus is the same as in Fig. 1; only the IP beta functions were reduced to $\beta_x^* = 6$ mm and $\beta_y^* = 70$ μm, by varying the strengths of 5 quadrupoles located at the final-focus entrance. The free length to the IP is again $l^* = 4.3$ m. However, the value of the radiation integral has increased to $I_5 \approx 2\times10^{-19}$ m, indicating an emittance growth of

$$\Delta(\gamma\epsilon_x) \approx (4\times10^{-8}\ \mathrm{m^2\ GeV^{-6}})E^6 I_5 \approx 90\ \mathrm{nm}\ , \quad (3)$$

which is near the tolerable limit.

Comparing Figs. 1 and 2, we may ask whether reducing the length of the energy collimation is acceptable. To answer this question, several criteria need to be taken into account. In addition to the overall length of the system, these are the impact on the simulated luminosity performance, the possible loss in collimation efficiency, and, to a lesser extent, the magnitude of the collimator wake fields. Finding an adequate tradeoff between the various requirements is difficult.

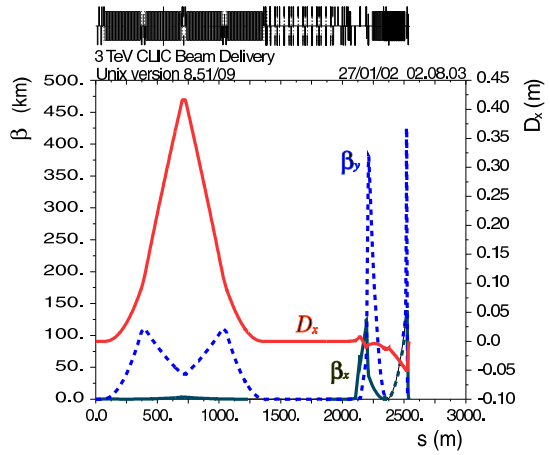

Figure 2: Optics of 3-TeV beam delivery system with shortened collimation section and squeezed IP beta functions, as of January 2002

3.2 3-TeV Performance

The simulated 3-TeV luminosity performances for collimation systems of different lengths and bending angles are compiled in Table 2. As for the luminosity studies mentioned in the previous section, these simulations were performed using an upgraded version of MAD8 [7, 8] (exact transformation through field-free regions). Here, 10000 particles were tracked through the entire beam delivery, and the luminosity at the collision point was computed by allocating charges to a grid. Hourglass effect and pinch were not taken into account, neither magnet errors or wake fields. The results were cross-checked against PTC [9] and several other simulation codes [10].

Shortening the system length by a factor 2.4 has decreased the luminosity by about 10% (compare the top and bottom rows of numbers). This does not seem to be too high a prize for a significant saving in real estate. The two intermediate cases were obtained by either re-inserting the other half of the energy collimation or re-scaling the bending angles and lengths to those of the longer system (center rows). They appear less favorable and show even lower luminosities than the present short system.

The momentum bandwidth and the contributions from synchrotron radiation in dipoles and quadrupoles for the compact beam delivery system are illustrated in Fig. 3, which depicts the simulated luminosity (once more without pinch and hourglass, but see Fig. 4) relative to the ideal value (linear-optics) L_0 as a function of the momentum full-width. The simulations were again performend with the upgraded version of MAD8, but, in this case, a flat uniform momentum distribution was considered.

The figure shows that both synchrotron radiation and energy spread significantly degrade the luminosity. The nominal full-width momentum spread is about 1%. Closer inspection and additional simulations reveal that the syn-

Table 2: Lengths and luminosities for various collimation systems at 3 TeV; the IP beta functions were held constant at $\beta_x^* = 6$ mm, $\beta_y^* = 70$ μm.

system	length [m]	luminosity w/o pinch $[10^{34}]$ cm^{-2}s^{-1}]
present (Fig. 2)	2557	3.98
2× energy coll.	4325	3.80
increase length by 1.6 & reduce θ_b by 3/8	3356	3.76
2× energy coll. & incr. length & red. θ_b (optics of Fig. 1)	6186	4.46

chrotron radiation in bending magnets causes about a luminosity loss by about a factor of 2, the momentum spread a 30% loss, and synchrotron radiation in the final quadrupoles a further 10% loss.

On the other hand, squeezing the IP beta functions from $\beta_x^* = 8$ mm and $\beta_y^* = 150$ μm to $\beta_x^* = 6$ mm and $\beta_y^* = 70$ μm yields a luminosity improvement of about 10%, thereby approximately compensating for the luminosity loss brought about by shortening the collimation system.

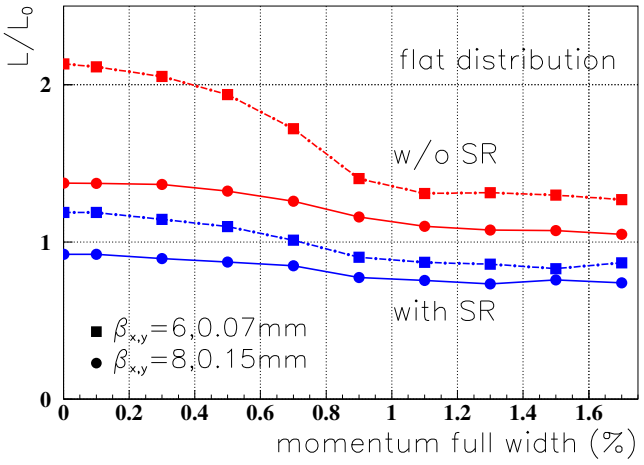

Figure 3: Simulated luminosity without hourglass and pinch effect as a function of the full-width momentum spread, with and without synchrotron radiation, for two different values of $\beta_{x,y}^*$ and assuming $\gamma\epsilon_y = 10$ nm. The luminosity is normalized to the target design luminosity, $L_0 = 4.6 \times 10^{34}$ cm^{-2}s^{-1}.

Simulations of the luminosity performance were also performed including pinch, beamstrahlung, and pair production during the collision. Beamstrahlung leads to an energy loss, which lowers the centre-of-mass energy for subsequent electron-positron collisions. For CLIC parameters, only about a third of the total luminosity is found within 1% of the nominal design energy [11]. Figure 4 presents this fraction of the simulated luminosity as a function of the two IP beta functions. This figure is the result of an integrated simulation with PLACET [12] and Guinea-Pig [13], modelling the particle transport from the entrance of the BDS through the collision.

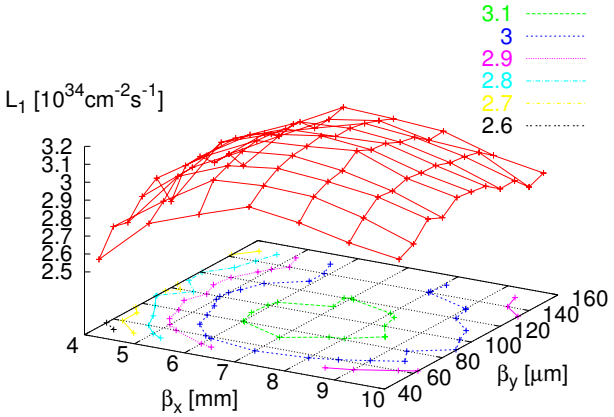

Figure 4: 3-TeV luminosity L_1 ($E_{\rm cm} > 99\%E_0$) with pinch, beamstrahlung and pair production vs. β_x^* & β_y^*, as determined by integrated simulations using PLACET and Guinea-Pig .

3.3 *500-GeV Optics*

The optics for 500 GeV is obtained by minor modifications to the 3-TeV system. It is shown in Fig. 5.

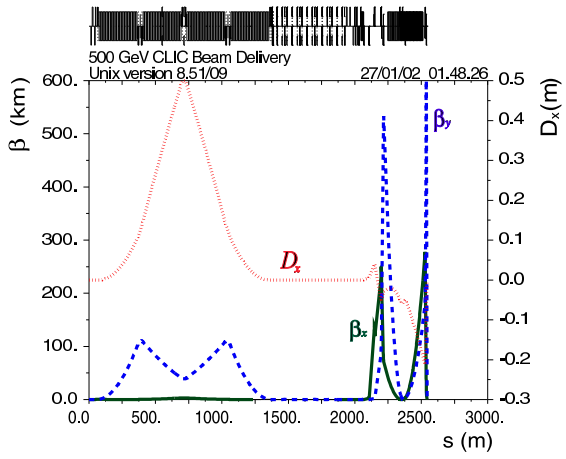

Figure 5: Optics of 500-GeV beam delivery system.

The total system length is the same, but the bending angles and the dispersion function in the final focus are 4.25 times larger than at 3 TeV (the sextupole fields are correspondingly reduced). In the energy collimation section, the bending angles and dispersion are also increased, but

only by a moderate 20%. Because the Oide effect is much weaker at 500 GeV, the beta functions at the IP can be squeezed further than at 3 TeV, down to values as small as $\beta_x^* = 3$ mm, and $\beta_y^* = 50$ μm. The IP distribution then becomes distinctly non-Gaussian and the rms beam size is no longer a good indication of the luminosity.

3.4 500-GeV Performance

Table 3 shows that, in the tracking simulation, for constant emittances at the entrance of the final focus, the geometric luminosity without pinch increases from $L = 1.02 \times 10^{34}$ cm^{-2} s^{-1} for $\beta_y^* = 150$ μm, $\beta_x^* = 10$ mm, to $L = 1.85 \times 10^{34}$ cm^{-2} s^{-1} for $\beta_y^* = 50$ μm, $\beta_x^* = 3$ mm (at 200 Hz with $\gamma\epsilon_y = 10$ nm). This is almost twice the desired target value. Also for 500 GeV, the luminosity with pinch was inferred from integrated simulations [14, 11], which show that reducing only β_y^* and leaving β_x^* at 10 mm preserves the quality of the luminosity spectrum. This corresponds to a luminosity (w/o pinch) of 1.5×10^{34} cm^{-}2s^{-1}.

Table 3: Effect of varying $\beta_{x,y}^*$ at 500 GeV on the rms spot sizes $\sigma_{x,y}$ and the luminosity without pinch for a 200-Hz repetition rate, $n_b = 154$ bunches/train, and $N_b = 4 \times 10^9$. When reducing $\beta_{x,y}^*$, the rms spot size no longer reflects the effective beam size which determines the luminosity.

$\gamma\epsilon_y$ [nm]	β_y^* [μm]	β_x^* [mm]	σ_x [nm]	σ_y [nm]	L [10^{33} cm^{-2} s^{-1}]
20	150	10	209	2.65	7.3
10	150	10	209	1.88	10.2
10	110	10	209	1.69	11.5
10	70	10	209	1.55	13.6
10	50	10	209	1.56	15.0
10	50	8	189	1.77	16.0
10	50	6	169	2.17	17.2
10	50	4	160	3.12	18.1
10	50	3	178	4.07	18.5

3.5 Beta Squeeze

As shown above, for CLIC the reduction in the vertical IP beta function to values much below those of other linear collider designs yields a higher luminosity (this is not the case, e.g., for NLC [15]). This beta squeeze is facilitated by the Raimondi final focus, thanks to its wide bandwidth and good chromatic properties. It also makes optimum use of the short bunch length in CLIC (far from the hourglass limit), and of the decreased vertical emittance (*i.e.,*, reduced impact of aberrations, lower divergence at the IP). As a side effect of the small beta functions, the computed rms spot sizes become less meaningful. Instead, an effective beam size can be obtained from a Gaussian fit to the simulated particle distribution at the IP [16] or from the luminosity spectrum of the beam-beam simulation [11]. The two approaches give compatible results.

3.6 Footprints

Figure 6 shows the footprints of the two beam delivery systems for 3 TeV and 500 GeV, respectively. The maximum horizontal separation between the two beamlines is about 20 cm, and an initial bending section, or an inversion of the deflection angle in the collimation system, will be required to make both entrance and collision points of the two systems coincide.

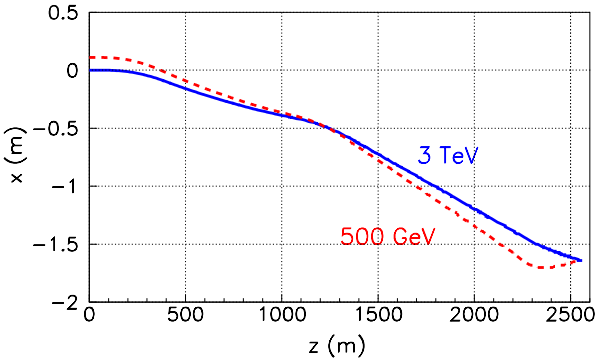

Figure 6: Footprints of the 3-TeV and 500-GeV beam delivery systems.

3.7 Recipe for Compact Final Focus

To stimulate the discussion at the workshop, we presented a draft procedure for the design of a compact final focus consisting of the following steps: (1) design a linear system with dispersion across the final doublet (FD); (2) add 2 sextupoles near the FD, correct the vertical chromaticity ξ_y and the second order dispersion T_{166}; (3) adjust the horizontal linear optics upstream to cancel ξ_x as well; (4) add 2 or 3 geometric sextupoles upstream, and cancel the second order geometric aberrations T_{122} and T_{144}; (5) minimize higher order aberrations by fine-tuning of $\alpha_{x,y}$ and phase advances, adding octupoles, modifying the dispersion, etc.

Inspired by the design scheme applied for ATF-II, we have meanwhile analyzed the 3rd order aberrations in a generic compact final focus using Lie algebra, and then, following the ATF-II example, designed a compact final focus for CTF-3. This system and the new design recipe adopted are described in a companion paper [17]. Differences of the CTF-3 final-focus design approach to that sketched above are that for CTF-3 we have strictly matched to pseudo $-I$ transformations between the two sextupoles for each of two interleaved sextupole pairs, that the 3rd order optical aberrations (namely the sum $(U_{3224}^2 + U_{3444}^2)$ in Transport notation) were minimized by adjusting the strength of the final quadrupole, and that we have accepted a large nonzero dispersion at all sextupoles. This modified design recipe remains to be applied to the CLIC final focus.

4 INTERACTION REGION

4.1 Overview

A schematic of the CLIC interaction region is displayed in Fig. 7. A strong solenoid field of strength 4–6 T occupies the inner ±(2–3) m around the collision point. The final quadrupoles are located 4.3 m away from the IP, and, hence, are more than 1 m outside of the solenoid field. This should minimize harmful interference, if, as foreseen, these quadrupoles are made from permanent magnets. As indicated in the figure, the beams are crossed under a horizontal angle, so that sufficient transverse space is available in the spent-beam path. Crab cavities must be used to avoid an otherwise unacceptable loss in luminosity due to the crossing angle.

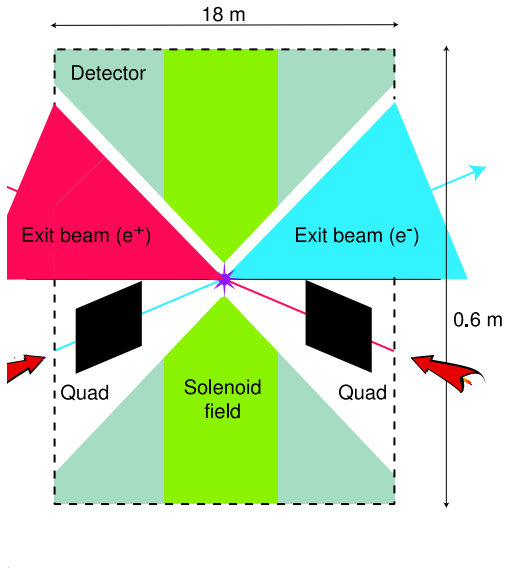

Figure 7: Top view of the CLIC IP region with the detector, the colliding beams, and the final quadrupoles at 3 TeV [18]. Scales are indicated. The transverse size of the detector is about 17 m.

4.2 Crossing Angle, Solenoid, and Crab Cavity

The full crossing angle θ_c must be chosen equal to or larger than 20 mrad, accounting for the divergence of the spent beam at 3 TeV [19]. The same limit of $\theta_c \geq 20$ mrad is set by the multi-bunch kink instability [20, 21], if one includes the effect of coherent pairs [22]. On the other hand the crossing angle cannot be chosen too large, or $\theta_c \leq 20$ mrad, in order to confine the vertical beam-size blow up due to synchrotron radiation in the solenoid (fringe) field together with vertical dispersion induced by the combination of crossing angle and solenoid [22]. This last aspect is illustrated in Fig. 8. Hence, at 3 TeV the crossing angle is uniquely determined.

For the nominal crossing angle of 20 mrad, a crab cavity voltage of

$$\hat{V}_{\rm crab} = \frac{\theta_c E}{2R_{12} e k_{\rm rf}} \approx 1 \text{ MV} \qquad (4)$$

is required, assuming that the crab cavities are operated at 30 GHz; at a lower rf frequency a higher voltage is needed (here E is the beam energy, R_{12} the R-matrix element from the cavity to the IP, and $k_{\rm rf}$ the rf wave number; we have assumed $R_{12} \approx 23$ m [23]). The relative phase of the two crab cavities on either side of the IP must be stabilized to within $\Delta\phi_{lr} \leq 0.06°$, to limit the luminosity loss to less than 2%. This phase tolerance (in units of degree) is tighter for lower frequencies ($\Delta\phi_{lr} \propto 1/\lambda_{\rm rf}$).

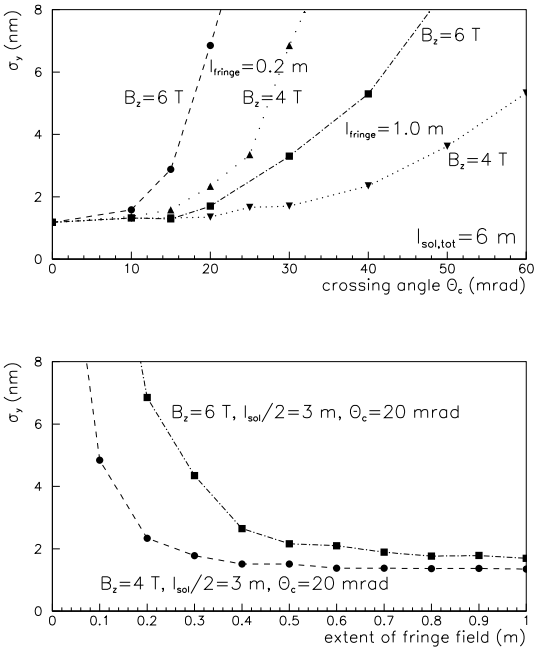

Figure 8: Vertical spot size σ_y^* as a function of the full crossing angle θ_c (top) and the extent of the fringe field (right), for solenoid field strengths of 4 and 6 T.

It is interesting to note that the combined effect of solenoid, crossing angle, and crab cavity will reduce the effective collision time, or — phrased differently — increase the projected beam size, even in the complete absence of synchotron radiation. In the following we discuss the mechanism of the luminosity degradation and estimate its magnitude.

We first derive the transformation describing the particle propagation from the beginning of the solenoid fringe field to the IP. We simplify the problem, by considering a solenoid with a hard-edge fringe. Then, at the entrance of the solenoid a particle receives the transverse deflection

$$\Delta x' = \frac{B_s y_s}{(B\rho)} \qquad (5)$$

$$\Delta y' = -\frac{B_s x_s}{(B\rho)}\,, \qquad (6)$$

where the transverse coordinates x_s and y_s describe the transverse position with respect to the symmetry axis of the solenoid. Defining $K \equiv ecB_s/E$ the motion inside the solenoid is conveniently described in a rotating frame [24]

$$u \;=\; e^{\frac{iKs}{2}}(x+iy)\;, \tag{7}$$

where the equation of motion simplifies to

$$u'' + \frac{K^2}{4}u \;=\; 0\;. \tag{8}$$

The solution is

$$u \;=\; u_0\cos\frac{K}{2}s + u_0'\frac{2}{K}\sin\frac{K}{2}s \tag{9}$$

where

$$u_0 \;=\; x_0 + iy_0\;, \tag{10}$$

$$u_0' \;=\; x_0' + iy_0' + i\frac{K}{2}(x_0+iy_0)\;, \tag{11}$$

and the subindex 0 refers to the transverse particle coordinates just behind the entrance edge of the solenoid, measured with respect to the solenoid axis. The final vertical coordinate at the longitudinal position s inside the solenoid (counted from the solenoid entrance) is obtained by transforming back to the original coordinates:

$$\begin{aligned} y^* &= \mathrm{Im}[e^{-i\frac{Kl}{2}}u] \qquad (12)\\ &= y_0 + \frac{2}{K}\left(y_0'\cos\frac{Ks}{2}\sin\frac{Ks}{2} - x_0'\sin^2\frac{Ks}{2}\right)\;. \end{aligned}$$

In the following, l denotes the the solenoid half length. We further find it convenient to introduce the initial coordinates just prior to the solenoid fringe, x_i, y_i, x_i' and y_i', which are defined with respect to the axis of the beam line. An ideal unperturbed distribution would be a Gaussian in these 4 phase-space variables. Considering a particle which crosses the center of the solenoid at $s = l$, and taking into account the crossing angle θ_c and the deflection by the solenoid fringe field, the initial coordinates and those after the entrance edge (x_0, x_0', y_0, y_0') are related via

$$x_0' \;=\; x_i' + \frac{\theta_c}{2} + \frac{K}{2}y_i\;, \tag{13}$$

$$y_0' \;=\; y_i' - \frac{K}{2}\left(-l\frac{\theta_c}{2} + x_i\right)\;, \tag{14}$$

$$x_0 \;=\; l\frac{\theta_c}{2} + x_i\;, \tag{15}$$

$$y_0 \;=\; y_i\;. \tag{16}$$

It is now easy to demonstrate that for a collision point located at $s = l$, the effect of the crossing angle approximately cancels, provided that $\phi \equiv (K/2)l \ll 1$. Namely, making this last assumption, Eq. (12) becomes

$$\begin{aligned} y^* \;\approx\; & y_0 + sy_i' - s\frac{K}{2}x_i + sl\frac{K\theta_c}{4} - s^2\frac{K}{2}x_i' \\ & -s^2\frac{K\theta_c}{4} - s^2\frac{K^2}{4}y_i\;. \end{aligned} \tag{17}$$

The crab cavity applies a dipole deflection to each particle such that the beams effectively collide head on. As a consequence particles at the head or tail of the bunch do not pass through the center of the solenoid, and the above cancellation is not exact during the full length of the collision. Consider a particle at a distance z ahead of the bunch center, and, for simplicity assume that the R_{22} matrix element from the crab cavity to the IP is zero. At $s = l$ this particle will be offset horizontally by $\Delta x^* = -z\theta_c/2$. The corresponding additional horizontal displacement at the entrance of the solenoid is $(-z\theta_c)(1 - lR_{22}/R_{12})$, where R_{12} and R_{22} denote the optical transport matrix elements from the crab cavity to the IP. Due to the deflection in the solenoid fringe field, this term gives rise to an additional vertical displacement at the IP of $\Delta y^* = \frac{K\theta_c}{4}z(1 - lR_{22}/R_{12})$. It is zero if $lR_{22} = R_{12}$, as would be the case, *e.g.*, for $R_{12} = l$ and $R_{22} = 1$. We introduce the abbreviation

$$C \equiv (1 - lR_{22}/R_{12})\;. \tag{18}$$

Including the vertical displacement imparted by the horizontal crab cavity, and further taking $y_i' = x_i' = y_i = 0$, the vertical offset at location s inside the solenoid follows from (17) as

$$\Delta y_1^*(z_1, s) \approx \frac{sK\theta_c}{4}(Cz_1 - s + l)\;. \tag{19}$$

We assume that this first particle belongs to beam 1 (subindex 1), and take $z_1 = s - l - ct$. A particle at position $z_2 = -(s-l) + ct$ in the opposing beam (subindex 2) experiences a deflection in the opposite direction,

$$\Delta y_2^*(z_2, s) \approx -\frac{(2l-s)K\theta_c}{4}(Cz_2 + s - l)\;. \tag{20}$$

so that the distance between the two beams 1 and 2 is

$$\begin{aligned} \Delta &\equiv \Delta y_1^*(s, z_1) - \Delta y_2^*(s, z_2) \\ &= -\frac{lK\theta_c}{2}Cct + \frac{lK\theta_c}{2}(C-1)(s-l)\;. \end{aligned} \tag{21}$$

To illustrate the loss in luminosity that may arise if $C \neq 0$, we consider the example $R_{22} = 0$ or $C = 1$. In this case, the vertical displacement varies linearly with time t, and is otherwise independent of s and z. For $t = 0$ the two entire beams are at the transverse center of the solenoid and the beams collide head on. At all other times, there is a non-vanishing vertical displacement Δ. The instantaneous luminosity reduction due to the displacement becomes

$$\begin{aligned} \frac{L(t)}{L_0(t)} &= \exp\left(-\frac{\Delta^2}{4\sigma_y^2}\right) \\ &= \exp\left(-\frac{(lK\theta_c ct/2)^2}{4\sigma_y^2}\right)\;, \end{aligned} \tag{22}$$

and the total reduction, integrated over the collision is

$$\begin{aligned} \frac{L}{L_0} &= \frac{c}{\sqrt{\pi}\sigma_z}\int_{-\infty}^{\infty} dt\ \exp\left(-\frac{(lK\theta_c ct)^2}{16\sigma_y^2}\right) \\ &\qquad \exp\left(-\frac{(ct)^2}{\sigma_z^2}\right) \;=\; \frac{1}{\sqrt{1 + \frac{(\sigma_z lK\theta_c)^2}{16\sigma_y^2}}}\;. \end{aligned} \tag{23}$$

For example, inserting $l = 3$ m, $\theta_c = 20$ mrad, $\sigma_z = 30$ μm, $B_s = 6$ T, and $E = 1.5$ TeV, we obtain $L/L_0 \approx 0.85$, or a 15% loss in luminosity. This shows that the effect of the crab cavity and the solenoid requires a precise compensation scheme. For lower beam energies, and the same solenoid field and crossing angle, the luminosity loss will be larger.

A possible cure would be to steer the beam with a vertical slope so as to compensate the average downward (or upward) motion during the collision, and at the same time to employ a vertical crab cavity in order to correct the resulting vertical beam tilt. In the general case of arbitrary C, the vertical crab cavity should apply a deflection

$$\Delta y_0'(z) = \frac{K}{2} C R_{12} \Delta x_0'(z) \; , \qquad (24)$$

which is proportional to the deflection imparted by the horizontal crab cavity, $\Delta x_0'(z)$, and exactly cancels the purely time-dependent term in Eq. (21). One approach to realizing the vertical crab deflection is to rotate the horizontal crab cavity by an angle $KCR_{12}/2$.

4.3 *Final-Quadrupole Design*

Two final quadrupoles based on the permanent-magnet material Sm_2Co_{17} have been designed using the ROXIE program [25]. The stronger magnet achieves a gradient of 467.5 T/m, the other the nominal gradient of 388 T/m [25] required by the present optics. Much weaker magnets would be needed at 500 GeV. Quadrupole parameters for both magnets are compiled in Table 4. A magnetic field-map for the cross section of the stronger of the two quadrupole designs is shown in Fig. 9.

Table 4: Final-quadrupole parameters for two designs [25].

length	4.75 m	3.5 m
field gradient	468 T/m	388 T/m
inner radius	3.3 mm	3.8 mm
outer radius	20 mm	43 mm
weight	50 kg	150 kg
p.m. material	Sm_2Co_{17}	
radiation hardness	$\Delta B/B \leq 0.4\%$ at 2 MGy	
damage threshold for neutrons	$> 10^{18}$ n cm^{-2}	
temperature stability	3×10^{-4} K^{-1}	

We assume that the permanent-magnet field cannot be varied and that the IP beta functions are adjusted using upstream quadrupoles. The squeezing of the IP beta functions described in Section 3.4 was effected in this way.

4.4 *Multipole Content*

Table 5 lists relative harmonic field errors for the preliminary design of the two permanent-magnet quadrupoles and for one of the chromatic correction sextupoles [25]. If the

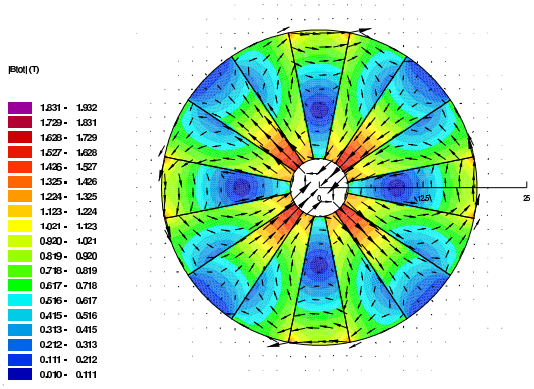

Figure 9: Cross section of a final focusing quadrupole with gradient 468 T/m based on the permanent magnet material VACOMAX 225HR Sm_2Co_{17}, as computed for a 16-sector magnet by ROXIE [25].

nth order multipole error b_n of a quadrupole remains uncompensated, the vertical spot size increases by

$$\frac{\Delta\sigma_y^*}{\sigma_{y0}^*} \approx (n-1)\sqrt{(2n-5)!!}\,\frac{G L_Q b_n}{(B\rho) r_0^{n-2}}\,\beta_{Q,x}^{\frac{n-2}{2}}\,\epsilon_x^{\frac{n-2}{2}}\,\beta_{Q,y} \; ,$$

where $\beta_{Q,x(y)}$ denotes the horizontal (vertical) beta function at the center of the magnet, L_Q is the magnet length, G the gradient in T/m, and $(B\rho)$ the magnetic rigidity. Inserting the values of Table 5 the relative beam-size blow up from the quadrupole b_4 field errors is less than 0.06% and that from the sextupole b_5 error about 0.01%.

Table 5: Relative harmonic field errors for 16-segment quadrupoles and 24-segment sextupoles at $r_0 = 2.2$ mm in units of 10^{-4}, with 1 mm stainless steel support pipe.

	quad. 1	quad. 2	sext.
strength	467.5 T/m	398.2T/m	90kT/m^2
b4	0.035	0.0003	0
b5	0	0	0.446
b6	0.109	-0.323	0
b7	0	0	0.519
b8	-0.002	-0.0001	0

4.5 *Resistive-Wall Wake Field*

The beam-pipe radius in the final quadrupoles is small (3.8 mm at the minimum), in order to produce the desired gradient. Therefore, resistive-wall wake fields become a concern. The centroid deflection due to the resistive wall is

$$\langle \Delta y' \rangle = 0.3\,\frac{2}{\pi}\,\frac{r_e N_b L}{a^3 \gamma}\,\left(\frac{c}{\sigma \sigma_z}\right)^{1/2} \langle y \rangle \; , \qquad (25)$$

where a is the radial aperture, σ the conductivity in s^{-1}, and the factor 0.3 arises from averaging over the longitu-

dinal bunch distribution. A figure of merit is the jitter enhancement K, given by

$$K \equiv \frac{\langle \Delta y' \rangle / \sigma_{y'}}{\langle y \rangle / \sigma_y} = 0.3 \frac{2}{\pi} \frac{r_e N_b L}{a^3 \gamma} \left(\frac{c}{\sigma \sigma_z} \right)^{1/2} \beta_y \ .$$

As an example, considering $\sigma = 5.4 \times 10^{17}$ s^{-1} (Cu), $a = 3.3$ mm, $E = 1.5$ TeV, $N = 4 \times 10^9$, $\sigma_z = 30$ μm, a length $L = 10$ m, $\beta_y = 400$ km, we find $K = 0.31$ (or a 5% enhancement if the motion in y and y' is uncorrelated).

4.6 Vacuum Aspects

The small chamber apertures might also compromise the pumping speed, possibly degrading the vacuum pressure. Local pumping may be accomplished either by using segments of permanent material with intermediate space, by a long slit along the magnet, or by coating with getter material [26]. To estimate the effect of the residual gas, we assume a train consisting of 154 bunches, each containing 4×10^9 electrons, which passes through 5 m of carbon monoxide gas at a pressure of 10 nTorr. The dominant scattering process is bremsstrahlung, with a cross section of 6.5 barn for an energy loss larger than 1% [27]. This yields 0.6 scattering events per bunch train.

4.7 Tolerances

In order not to degrade the luminosity by off-center collisions, a tight tolerance must be imposed on the vibrational motion of the final quadrupoles. Above 4 Hz this tolerance is a fraction of the IP spot size, or about 0.2 nm [1, 28]. On longer time scales the beam-beam collisions can be maintained by an interaction-point beam-beam deflection feedback.

More precisely, this tolerance refers to the stability of the magnetic center, which cannot only vary due to mechanical vibrations, but also due to a change in relative temperature between the two sides of the magnet [21]. For example, an asymmetric energy deposition of 9 kJ/m yields a relative temperature change by $\Delta T = 1$ K, that moves the vertical beam position by $\Delta y = 286$ nm [25], via the change in the magnetization, not taking into account the additional effect of thermal expansion. In principle, by properly combining different materials and choosing an adequate geometry, the thermal expansion can be made to counteract the change in magnetization. However, without such compensation, the acceptable limit on the asymmetric energy deposition is 6 J/m, which corresponds to a temperature difference of < 1 mK, to be maintained above 4 Hz. To put this into perspective, at 3 TeV the coherent pairs produced during the collision carry an energy of about 6 kJ per bunch train [21, 19].

5 COLLIMATION SYSTEM

5.1 Functions

The collimation system must fulfill a variety of functions. Primarily is should (1) remove beam halo to reduce detector background, (2) provide a distance between collimators and IP for muon suppression, (3) ensure collimator survival and machine protection, and (4) not amplify incoming trajectory fluctuations via the collimator wake fields.

5.2 Collimation Depth

The collimation depth for the CLIC betatron collimation is determined from the conditions that (1) beam particles and (2) synchrotron radiation photons emitted in the final quadrupoles should not hit any magnet apertures on the incoming side of the IP. Figure 10 shows synchrotron radiation fans emitted in the final doublet. The collimation depths should be less than $14\sigma_x$ or $83\sigma_y$ [1]. Due to nonzero dispersion across the final doublet, the number for the horizontal beam size σ_x includes both betatron and dispersive components, roughly equal in magnitude, such that the actual horizontal collimation depth at a place with zero dispersion needs to be $\sqrt{2}$ smaller, or about $10\sigma_x$. Scaling to lower energies, we need to replace the permanent final quadrupole by a weaker magnet. In principle, we could open up the aperture of this magnet like the inverse of the beam energy. This suggests that, for constant normalized emittances and beta functions, the collimation depth quoted in numbers of rms beam sizes could be increased in proportion to the inverse square root of energy. However, the horizontal normalized emittance does increase at 500 GeV, and both IP beta functions decrease somewhat. Therefore, for simplicity, we have assumed that the collimation depth in units of σ stays roughly constant, independent of the beam energy. However, recent background studies in the framework of the Technical Review Committee [29] indicate that, at 500 GeV, the direct impact of synchrotron radiation on the vertex detector could limit the permissible collimation depth to smaller values.

On the other hand, the energy collimation depth is not determined by the background, but instead it is set by failure modes in the linac, to a value of about $\pm 1\%$ or $\pm 1.5\%$ [30]. This setting ensures, for all failure scenarios studied, that mis-steered or errant beams will either hit the energy spoiler, where the beam size is sufficiently large for collimator survival, or will pass all the way through the interaction point, without impacting on a betatron collimator.

5.3 Collimator Survival

As in other designs the collimators consist of pairs of short spoilers and long absorbers. Scattering of a mis-steered beam by a spoiler increases the beam size at the absorber. Even with this precaution, passive survival of the collimators is a concern, especially for the spoilers. In Fig. 11, the design beam sizes at spoiler locations in the energy collimation section, the betatron collimation section, the com-

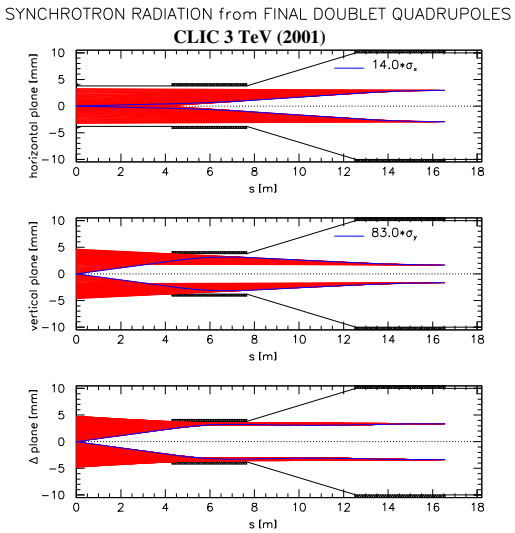

Figure 10: Synchrotron radiation fans at 3 TeV with beam envelopes of $14\sigma_x$ and $83\sigma_y$ [Courtesy O. Napoly] [1].

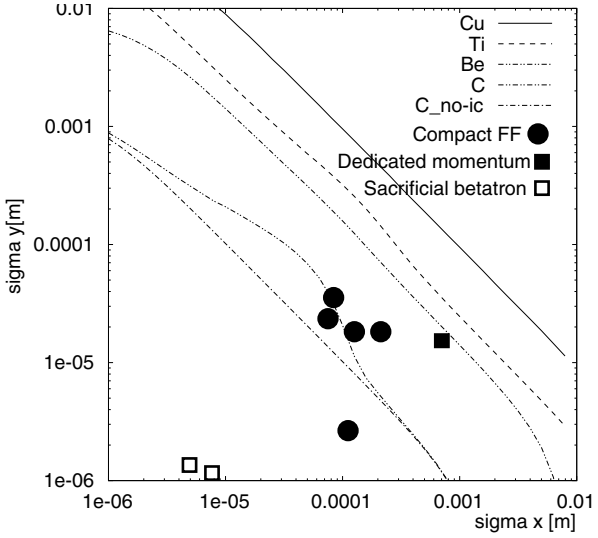

Figure 11: Vertical vs. horizontal beam size required for spoiler survival and values at spoiler locations [31], and typical values at prospective spoiler locations in the 3-TeV CLIC beam delivery system, as computed from the design beta functions, emittances and energy spread.

pact final focus, and the alternative baseline final focus are superimposed on spoiler survival curves for various materials, which take into account the energy deposition by both ionization and by image current ohmic heating [31]. For the present short energy collimation section, the rms radial beam size $\sigma_r \equiv \sqrt{\sigma_x\sigma_y}$ is 108 μm at the spoiler, assuming nominal emittances and energy spread. Figure 11 illustrates that this should be sufficient to guarantee the survival of the momentum-collimation spoiler in the case of beam impact, provided that the spoilers are made from carbon or possibly beryllium [31]. We also note that the spoilers in the betatron collimation section are sacrificial, and will certainly be destroyed, if they are hit by a bunch train (for example, if the momentum collimators are not positioned properly).

The beam size at the momentum-collimation absorber is determined by the rms multiple scattering angle θ_0 in the preceding spoiler (0.5 radiation lengths) according to

$$\sigma_{r,\mathrm{ab}} = \sqrt{R_{12}R_{34}}\theta_0 \approx \sqrt{R_{12}R_{34}}\,\frac{13.6\ \mathrm{MeV}}{\beta cp}\,\frac{1}{\sqrt{2}}\,, \tag{26}$$

where R_{12} and R_{34} denote the transport-matrix elements between the spoiler and the absorber. In the present optics, $R_{12} \approx R_{34} \approx 165$ m, and $\sigma_{r,\mathrm{ab}} \approx 1.1$ mm. This is much larger than the limit for surface fracture, but still much smaller than a radiation length.

5.4 *Collimator Parameters*

The collimator parameters are summarized in Table 6.

Table 6: Collimator parameters.

cm energy	3 TeV	500 GeV
energy spoiler gap	$\pm$4 mm	$\pm$4.8 mm
β_x spoiler gap	$\pm$80 μm	$\pm$300 μm
	(10 σ_x)	(9 σ_x)
β_y spoiler gap	$\pm$104 μm	$\pm$215 μm
	(80 σ_y)	(69 σ_y)
spoiler material	Be (or C)	
spoiler length	177 mm (0.5 r.l. Be)	
	or 144 mm (0.5 r.l. C)	
absorber material	Ti (Cu coated)	Ti (Cu coated)
absorber length	712 mm (20 r.l.)	
no. of energy spoilers	1	
no. of $\beta_{x,y}$ spoilers	4, 4	

5.5 *Wake-Field Effects*

The deflection of the beam centroid by a tapered circular collimator is [32, 33]

$$\Delta y' = \frac{2N_b r_e}{\gamma\sigma_z}\left[\frac{(4\lambda\sigma_z)^{1/4}}{g^{3/2}} + \frac{L_F(\lambda\sigma_z)^{1/2}}{2\sqrt{\pi}g^3}\right] y \tag{27}$$

where y is the offset from the center of the chamber, $\lambda[\mathrm{m}] = \rho[\Omega\mathrm{m}]\,/(120\pi)$, L_F the length of the collimator flat part, and g the half gap. The taper angle is assumed to be optimally chosen as $\theta_{\mathrm{opt}} \approx 1.1(\lambda\sigma_z/g^2)^{1/4}$, such that the sum of the bunch centroid deflections due to geometric and resistive wake fields is minimized [32]. Equation (27) is correct for $\sqrt{\sigma_z\lambda} \ll g \ll \sqrt{\sigma_z\lambda}\sigma_z\,/\lambda$ [32], which, *e.g.*, for $\rho \approx 4\times10^{-8}\ \Omega$m evaluates to 60 nm $\ll g \ll$ 16 mm.

If the trajectory of the incoming beam changes, this change may be amplified by the collimator wake fields,

possibly resulting in an enhanced displacement at the interaction point (IP). For the 3-TeV design, we have computed the combined effect of 4 vertical spoilers and 4 absorbers located in the betatron collimation section. We here pessimistically assumed that the spoilers are made from uncoated beryllium and extend over 0.5 radiation lengths (r.l.), or 177 mm, and that the absorbers consist of copper-coated titanium with a length of 712 mm (20 r.l.). Note that solid copper would not be an adequate absorber material, since, even with protective spoilers upstream, copper could not withstand the stress induced by the impact of a bunch train [34].

The half gap of the collimators was set to $\pm 145\mu$m, or to $80\sigma_y$, assuming a normalized vertical emittance of 20 nm [3] (we recall that the present design value is 10 nm). For the vertical IP beta function of $\beta_y^* = 150$ μm considered in [3], this left a few σ margin [1] to ensure that all beamline elements downstream are shadowed by the collimators.

We computed the displacement at the IP for centroid trajectories with initial amplitude 1σ, considering bunches subjected to wake fields at the betatron spoilers and absorbers. The IP displacement depends on the betatron phase of the incoming oscillation. We always selected the betatron phase with maximum displacement. Figure. 12 displays the dependence of the maximum vertical IP displacement so obtained on the bunch population. From this figure we conclude that the jitter enhancement due to collimator wake fields is not a severe limitation. It is interesting that for certain values of beam current the centroid-beam jitter at the IP is strongly reduced. This can be understood by considering the effect of the collimator wake on the coherent beam motion like an additional quadrupole, and by realizing that for certain wake-field strengths the resulting 'coherent' beta function at the IP becomes smaller.

The result in Fig. 12 is independent of the length of the energy collimation section, since the latter does not contain vertical collimators. The result does, however, depend on the collimator gap. If, for the present design emittance of 10 nm and vertical IP beta function of 70 μm (both values are about two times smaller than those considered in Fig. 12), we maintain the collimation at 80 σ, the gap size g would be $\sqrt{2}$ times smaller (see Table 6), and, according to Eq. 27, the wake fields of the collimator taper and of the flat part would increase by factors 1.7 and 2.8, respectively. If needed, octupole magnets upstream of the final doublet, which 'fold in' the beam tails [35, 36, 37], could be employed to further increase the required collimation depth.

For the collimator gaps listed in Table 6, at 500 GeV the jitter enhancement due the spoiler wake fields is slightly lower than at 3 TeV, or

$$(\beta\Delta y'/y)_{500\mathrm{GeV}} \approx 0.8\,(\beta\Delta y'/y)_{3\mathrm{TeV}} \ . \qquad (28)$$

In addition to affecting the beam-centroid motion, the collimator wake fields also degrade the single-bunch emittance. The corresponding luminosity loss is between 2 and 8 times smaller than the luminosity loss caused by the centroid deflection [32]. Hence, for the nominal CLIC parameters this effect appears negligible.

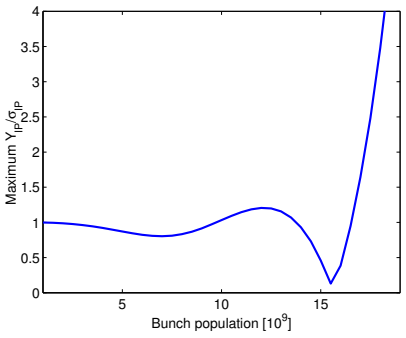

Figure 12: 'Maximum' IP orbit displacement for a 1σ change in incoming beam trajectory as a function of bunch population N_b, at 3 TeV, assuming collimation at 80 σ_y with $\gamma\epsilon_y = 20$ nm, and a beta function at the vertical collimators equal to 483 m.

6 NONLINEAR COLLIMATION

As an alternative to the baseline collimation system, described in Sections 3 and 5, a nonlinear system using three skew sextupoles has been explored [38]. The basic layout of this scheme is illustrated in Fig. 13. The purpose of the first skew sextupole, placed at a dispersive location, is to increase the vertical beam size at the spoiler. A single vertical spoiler follows about 90° in betatron phase advance behind this sextupole and collimates in all three degrees of freedom simultaneously. This should reduce the total length of the system, and minimize the wake-field effects. The skew sextupole also serves to amplify the beam centroid amplitude in case of a momentum error or an incoming horizontal betatron oscillation, thus allowing the positioning of the spoiler further away from the center of the beampipe, which also yields lower wake fields. A second skew sextupole downstream of the spoiler, and placed at a betatron phase advance of 180° from the first sextupole, cancels all aberrations induced by the former. The collimation for the orthogonal betatron phase, for which we assume much looser requirements, *i.e.*, larger collimation amplitudes, is accomplished by placing a third much weaker skew sextupole $\pi/2$ upstream of the first, in a region without dispersion.

In the actual optics, the horizontal dispersion tends to be small at the spoiler, $D_{\mathrm{sp}} \approx 0$. In principle, this is a desirable feature, which would avoid a coupling of energy errors into horizontal betatron oscillations via horizontal wake fields [6]. However, since in our scheme a spoiler is required only in the vertical direction, by design horizontal wake fields are absent, and the condition of zero horizontal dispersion is not necessary. Rather, a nonzero dispersion would increase the beam size at the spoiler, and improve the collimator survival.

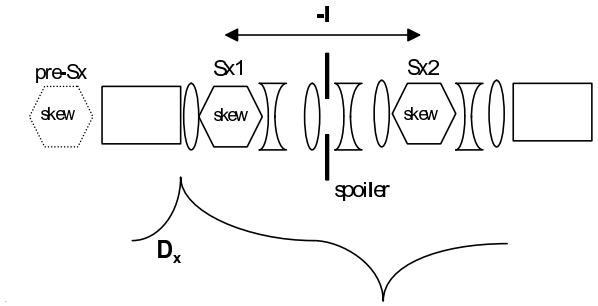

Figure 13: Schematic of the nonlinear collimation scheme.

An essential property of the system is the large beam size at the spoiler, designed to assure the collimator survival in case of beam impact. If we assume that the contributions from vertical beam size and emittance to the beam size at the spoiler are negligibly small compared with the contributions from the horizontal beam size and, especially, with those arising from energy spread and dispersion at the first main skew sextupole, the vertical beam size at the spoiler is approximated as [38]

$$\sigma_y \approx C_\delta \frac{1}{2} \, |R_{34} K_s| \, D_{\rm sext}^2 \delta_{\rm rms}^2 \; , \qquad (29)$$

where R_{12} and R_{34} denote the optical transport-matrix elements between the sextupole and the spoiler, $D_{\rm sext}$ is the dispersion at the skew sextupole, K_s is the integrated skew-sextupole strength, which can be expressed in terms of the sextupole length l_s, the pole-tip field B_T, the magnetic rigidity $(B\rho)$, and sextupole aperture a_s as

$$K_s = \frac{2 B_T l_s}{(B\rho) a_s^2} \; , \qquad (30)$$

and the factor C_δ is defined by $C_\delta \equiv \sqrt{<\delta^4>}/<\delta^2>$, where the angular brackets denote an average over the beam distribution. In case of a Gaussian distribution one finds $C_\delta = \sqrt{3}$, and in case of a flat distribution with sharp cutoff, which is more representative for a linear collider like CLIC, $C_\delta = \sqrt{9/5}$.

The horizontal beam size at the spoiler is determined from [38]

$$\begin{aligned} \sigma_x &\approx \left(R_{12}^2 K_s^2 D_{\rm sext}^2 \delta_{\rm rms}^2 \beta_{y,{\rm sext}} \epsilon_y + \beta_{x,{\rm sp}} \epsilon_x \right)^{1/2} \\ &\approx \left(\beta_{x,{\rm sp}} \epsilon_x \right)^{1/2} \; . \end{aligned} \qquad (31)$$

For spoiler survival, the beam size must be larger than a damage-threshold value $\sigma_{r,\min}$, such that $\sigma_y \sigma_x \geq \sigma_{r,\min}^2$, which we can rewrite as

$$C_\delta \frac{1}{2} \, |R_{34} K_s| D_{\rm sext}^2 \delta_{\rm rms}^2 \sqrt{\beta_{x,{\rm sp}} \epsilon_x} \geq \sigma_{r,\min}^2 \; . \qquad (32)$$

For a given value of $D_{\rm sext}$, Eq. (32), determines the minimum value of the product $|K_s R_{34}|$ required.

We denote the collimation amplitude for the horizontal and vertical betatron motion as $\pm n_x \sigma_x$ and $\pm n_y \sigma_y$, respectively, and the energy collimation depth in units of δ by $\pm\Delta$. A single vertical spoiler is employed to collimate in all three degrees of freedom. It is natural to produce a large horizontal beta function at the sextupole, since here the dispersion is large as well, and a large vertical beta function at the spoiler. The collimation of the horizontal motion and in energy then occurs via the nonlinear vertical deflection received at the skew sextupole. The vertical collimation is realized by adjusting the linear optics and the spoiler position in the usual way.

The beta functions follow from the required collimation amplitudes as

$$\beta_{x,{\rm sext}} = \frac{D_{\rm sext}^2 \Delta^2}{\epsilon_x n_x^2} \; , \qquad (33)$$

$$\beta_{y,{\rm spoiler}} = \frac{K_s^2 R_{34}^2 D_{\rm sext}^4 \Delta^4}{4 \epsilon_y n_y^2} \; . \qquad (34)$$

The three equations (32), (33), and (34) contain the product $|K_s R_{34}|$. Choosing K_s as large as possible and maintaining a reasonable pole-tip radius and $B_T \leq 1.4$ T, the minimum value of R_{34} is determined from $D_{\rm sext}$. The achievable value of the dispersion $D_{\rm sext}$ is limited by the emittance growth $\Delta(\gamma\epsilon_x)$ due to synchrotron radiation in the dipole magnets. The latter restricts the value

$$\Delta(\gamma\epsilon_x) \approx (4 \times 10^{-8} \; {\rm m}^2 \; {\rm GeV}^{-6}) E^6 I_5 < f \epsilon_x \qquad (35)$$

to a fraction f of the initial emittance. Here I_5 is the radiation integral [39], $I_5 = \sum_i L_i < \mathcal{H} > /|\rho_i|^3$, the sum runs over all bending magnets, with bending radius ρ_i, length L_i, and 'curly $\mathcal{H}$' function defined by Sands [40].

A solution to Eqs. (32), (33), (34), and (35) was found by adjusting the length of the collimation system, the beta functions, the dispersion, and the locations of sextupoles and spoiler.

Absorbers must intercept the particles that are scattered by the spoiler. One absorber can be located half a FODO cell behind the second skew sextupole, following the spoiler. This arrangement has the advantange that the scattered particles are further deflected by the strong skew sextupole before they impinge on the absorber. Although the location of the absorber is then more than 90° behind the spoiler, the R_{12} and R_{34} matrix elements between spoiler and absorber are still significant. A second absorber is placed 90° after the first one — which coincides with locations upstream and downstream of the bending magnets — such that both inwards and outwards scattered particles can be caught.

The phase advance to the collision point should be adjusted such that the two skew sextupoles described so far are located at a betatron phase that coincides (modulo π) with that phase of the final doublet, or is different by $\pi/2$ from that the collision point. The reason is that the required collimation depth in units of the rms beam size is much tighter for this phase than for the IP phase. In addition, much of the backgound is generated by particles traversing the final quadrupoles at a large amplitude, *i.e.*, in this betatron phase

The collimation depth in the ortoghonal betatron phase (IP phase) can be relaxed. and may be performed with a much weaker, single skew sextupole, which we locate upstream of the first strong skew sextupole. Particles at large amplitudes in the IP phase receive a nonlinear deflection which will displace them at the first main skew sextupole, where their deflection is amplified. They will then be collimated exactly as the particles in the final-doublet phase.

Denoting the $(3,4)$ transport matrix elements between the additional (pre-) skew sextupole and the first main skew sextupole by $R_{34}^{\rm pre}$, the collimation depths in units of σ for the IP betatron phase by $n_x^{\rm IP}$ and $n_y^{\rm IP}$, and the spoiler half gap by $a_{y,\rm sp}$, the strength of the additional skew sextupole is [38]

$$K_s^{\rm pre} = \frac{2}{{n_y^{\rm IP}}^2 \beta_y^{\rm pre} \epsilon_y} \left(\frac{2a_{y,\rm sp}}{K_s R_{34}}\right)^{1/2} \frac{1}{R_{34}^{\rm pre}}\,, \qquad (36)$$

which ensures that particles vertically offset by more than $n_y^{\rm IP}$ rms beam sizes will hit the spoiler. The horizontal collimation depth in the IP phase, $n_x^{\rm IP}$, is then fixed by

$$n_x^{\rm IP} = \left(\frac{2}{K_s^{\rm pre}\beta_x^{\rm pre}\epsilon_x}\,\frac{1}{R_{34}^{\rm pre}}\right)^{1/2} \left(\frac{2a_{y,\rm sp}}{K_s R_{34}}\right)^{1/4}\,, \qquad (37)$$

We assume that $n_y^{\rm IP}$ is so large and, hence, $K_s^{\rm pre}$ sufficiently small, that the geometric aberrations induced by this first skew sextupole need not be corrected. The residual relative blow up can be estimated as

$$\left(\frac{\Delta\sigma_{y'}}{\sigma_{y'}}\right)^{\rm pre} \approx \frac{\sqrt{3}}{2} K_s^{\rm pre}\beta_x^{\rm pre}\epsilon_x \sqrt{\frac{\beta_y^{\rm pre}}{\epsilon_y}}\,, \qquad (38)$$

to be added in quadrature, where the beta functions are those at the pre-sextupole.

The advantage of the described arrangement for orthogonal collimation is that it makes maximum use of the strong skew sextupoles already existing, and no additional spoilers are necessary.

Table 7 lists some beam parameters of CLIC at 3 TeV [41], which we have assumed for designing the nonlinear collimation system, as well as the collimation amplitudes [2].

Figure 14 presents the example optics. Its length is 2 km, hence comparable to that of the conventional linear system in Section 3. Pertinent parameters are compiled in Table 8. The rms spot size $\sigma_r \equiv \sqrt{\sigma_x\sigma_y} \approx 120$ μm is slightly larger than the corresponding value $\sigma_r \approx 108$ μm for the conventional system (see Figure 11) [31]. It is sufficient to guarantee spoiler survival, if the spoiler is made from carbon or possibly beryllium.

The value of the fifth synchrotron radiation integral is $I_5 \approx 1\times10^{-19}$ m, which amounts to an emittance growth of $\Delta(\gamma\epsilon_x) \approx 0.046$ μm, or about 7%, at 3 TeV. It is about half the value of the conventional system. However, this number does not include chromatic effects, which may further increase the luminosity degradation due to synchrotron radiation.

Table 7: Beam parameters and settings assumed for the nonlinear collimation system.

variable	symbol	value
beam energy	E	1.5 TeV
rms momentum spread	$\delta_{\rm rms}$	2.8×10^{-3}
hor. geom. emittance	ϵ_x	0.23 pm
vert. geom. emittance	ϵ_y	6.8 fm
hor. betatron coll. depth	n_x	10
vert. betatron coll. depth	n_y	80
energy collimation	Δ	0.013
hor. IP betatron coll. depth	$n_x^{\rm IP}$	460
vert. IP betatron coll. depth	$n_y^{\rm IP}$	2000

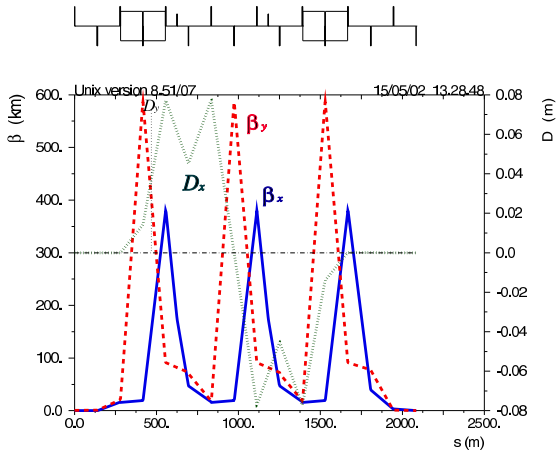

Figure 14: Optics of the nonlinear collimation system.

Finally, the blow up from the weak pre-sextupole, (38), is estimated as $\Delta\sigma_{y'}/\sigma_{y'} \approx 0.17$, which translates into a 2% increase for the rms vertical divergence at the IP.

So far the nonlinear-collimation optics does not include any chromatic correction. The chromaticity could be corrected either by adjusting sextupoles in the downstream final focus, or by locally adding dedicated normal sextupoles at high-dispersion points. However, the latter option might impair the cancellation of aberrations between the two strong skew sextupoles.

We plan to compare the performance and collimation efficiency of this nonlinear system with those of the linear design using the code BDSIM [42].

7 EXIT LINE

After the collision the beam acquires a significant angular spread. At 3 TeV, the particles emerging at largest angles are oppositely charged (coherent) pairs, requiring a free-space exit cone of at least ±10 mrad around the center line [19].

A second challenge posed by the spent beam in CLIC

Table 8: Optics parameters for nonlinear collimation

variable	value
length	2.07 km
beta functions (x, y) at skew sext.	175, 82 km
dispersion at skew sext.	61 mm
skew sextupole pole tip field	1.4 T
skew sextupole pole tip radius	4 mm
skew sextupole length	3 m
skew sextupole strength K_s	104 m^{-2}
R_{12}, R_{34} from sext. to spoiler	110, 307 m
beta functions (x, y) at spoiler	20.5, 586 km
dispersion at spoiler	$\sim$0 m
rms spot size (x, y) at spoiler	69, 209 μm
vertical spoiler half gap $a_{y,\mathrm{sp}}$	16.7 mm
hor. beta function at pre skew sext.	5.4 km
vert. beta function at pre skew sext.	19.5 km
dispersion at pre skew sextupole	0 mm
pre-skew sextupole pole tip field	23 mT
pre-skew sextupole pole tip radius	20 mm
pre-skew sextupole length	3 m
pre-skew sextupole strength K_s^{pre}	0.068 m^{-2}
R_{12} from pre-sext. to sext.	290 m
R_{34} from pre-sext. to sext.	113 m

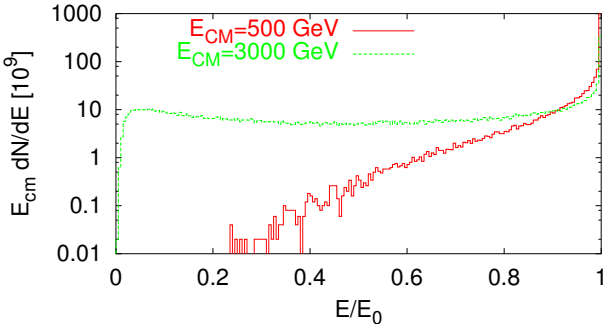

Figure 15: Energy distribution of the spent beam for centre-of-mass energies 3 TeV and 500 GeV, simulated using the code Guinea-Pig [19].

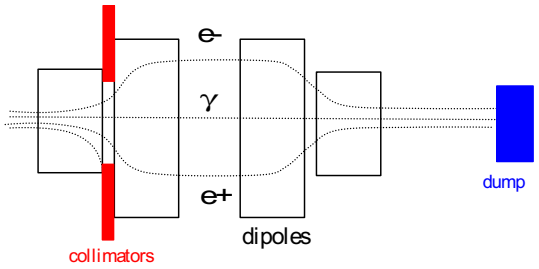

Figure 16: Schematic layout of a draft CLIC exit line which separates charged and neutral debris components using a chicane prior to disposal on a beam dump.

is its huge energy spread. This energy spread strongly increases for higher beam energies, as illustrated in Fig. 15. Note that the spent-beam characteristics is similar to that at a photon collider. It seems unlikely that a focusing optics can be found for a beam with nearly 100% energy spread. Hence, for the CLIC exit beam line we presently foresee only a simple chicane, which separates the charges and allows for diagnostics of the spent-beam energy spread. After the chicane the charged particle debris and the beamstrahlung photons are disposed onto a common beam dump. This scheme is illustrated in Fig. 16.

In order that the dump is not destroyed by the beam impact and also that the latter does not generate significant acoustic waves, a dump based on water at a nominal temperature 4°C (zero thermal expansion coefficient) is proposed [34].

8 SPIN TRANSPORT AND DEPOLARIZATION

The CLIC electron beam will be polarized. The orientation of the polarization vector at the collision point depends on its initial orientation at the entrance of the beam delivery system, on the beam parameters, and on the optical transport. The magnitude of the polarization vector can shrink due beam transport with a finite energy spread and nonzero transverse emittance.

The spin propagation for an individual particle is described by the Thomas-BMT equation:

$$\frac{d\vec{S}}{dt} = \frac{e}{\gamma m}\vec{S} \times \left[(1+a\gamma)\vec{B}_{\perp} + (1+a)\vec{B}_{||}\right] \qquad (39)$$

where $a = (g-2)/2 = 0.00115966$ denotes the anomalous magnetic moment of the electron. For similar field strengths, the spin rotation and depolarization could be larger at higher energy (larger γ).

The spin transport in the CLIC beam delivery was estimated using numerical tracking [44]. We considered a distribution of N particles, and defined a classical spin vector $\vec{S}_i$ for each particle. The particles were then tracked through the beam delivery at the nominal beam energy of 1500 GeV, corresponding to $a\gamma = 3404$. Transverse fields that deflect the particle by an angle θ cause a spin rotation, which is $a\gamma = 3404$ times larger. For simplicity we approximated the factor $(a\gamma + 1)$ for quadrupoles by $a\gamma$, which introduces a negligible error, as long as $\theta \ll 1$. Taking into account all transverse fields (bending magnets and quadrupoles) in the beam delivery system, the rotation of the individual spin vectors was calculated using Eq. (39). The polarization vector is then obtained as the average of all individual spin vectors:

$$\vec{P} = \begin{pmatrix} P_x \\ P_y \\ P_z \end{pmatrix} = \frac{1}{N} \sum_{i=1}^{N} \vec{S}_i \ , \qquad (40)$$

and the degree P of polarization is determined by the length of the polarization vector:

$$P = |\vec{P}|. \qquad (41)$$

For the spin tracking studies, we considered the previous version of the CLIC beam delivery system, shown in Fig. 1, which consists of the present compact final focus, and a 5.5-km long extensive collimation system.

We tracked 10000 particles using the MAD program [7], and obtained the phase-space coordinates behind each beam-line element. In a second step, we computed the evolution of the single-particle spin vectors and their average from the individual phase-space trajectories.

The initial particle coordinates chosen are representative of the CLIC beam. In the transverse phase space the particle distributions were taken to be Gaussians with rms beam sizes corresponding to the emittances of $\gamma\epsilon_x = 0.68$ μm and $\gamma\epsilon_y = 0.02$ μm (*i.e.*, the vertical emittance was two times larger than for the present design). In the longitudinal phase space, we assumed a Gaussian spatial profile as well (irrelevant for this study) and a flat energy spread extending from -0.4% to $+0.4\%$, which is a fair approximation to the shape predicted by linac simulations [45].

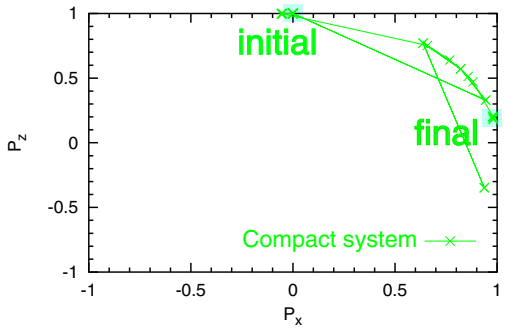

Figure 17: Rotation of the polarization vector in the x-z plane in the CLIC beam delivery system of Fig. 1. The initial ($P_x = 0, P_z = 1$) and final polarization values are indicated by underlaid boxes.

The rotation of the polarization vector in the x-z plane is shown in Figure 17. All particles start with a longitudinal spin vector $S_i = (0, 0, 1)$, therefore $P_z = 1$ initially. For physics purposes the polarization vector should point into the longitudinal z-direction at the collision point. Due to the design dipole fields, it is, however, strongly rotated into the horizontal direction, leaving a very much reduced level of longitudinal polarization ($P_z < 50\%$). It is evident that the polarization vector must be "matched" into the beam delivery system, requiring specific non-zero values for the initial horizontal and longitudinal polarization components.

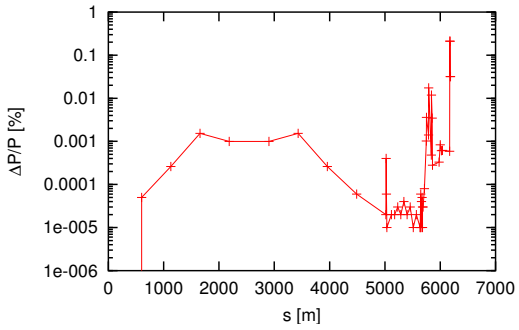

Figure 18: Depolarization versus longitudinal position s due to the transverse magnetic fields in the CLIC beam delivery system of Fig. 1.

The beam can be depolarized if the individual particle spins are rotated differently. This happens due to the final beam size in the quadrupoles (particles at small amplitudes are almost unperturbed, while particles at large amplitudes in the tails of the beam can experience strong spin rotations) or due to beam energy spread in the bending magnets. We calculated the depolarization due to these two effects. The results are shown in Fig. 18. As expected, the depolarization is strongest at the final doublet, where the spot size and the quadrupole strengths are largest. The final net depolarization is about 0.03%. Hence, the expected depolarization from transverse fields in the CLIC BDS is small and can be neglected for practical purposes.

9 CONCLUSIONS

The present design of the CLIC beam delivery system performs well both at 3 TeV and at 500 GeV. In simulations without errors, the 500-GeV system exceeds the target luminosity without pinch, 10^{34} cm^{-2}s^{-1}, by a factor 1.5. The simulated 3-TeV luminosity (without pinch) is close to the target value of 4.6×10^{34} cm^{-2}s^{-1}.

If not properly taken care of, several small and subtle effects could degrade the attainable performance. Prominent among these effects is the luminosity loss due to the relative vertical motion induced by crab cavity, solenoid, and crossing angle.

An alternative nonlinear collimation system has been designed, for which beam sizes, emittance growth, and system length all appear comparable to the conventional system. One advantage may be the much smaller collimator wake fields (a 17-mm collimator half gap, compared with 100 μm half gaps for the conventional design).

A draft design procedure for a compact final focus system has been proposed. Recent progress by the CLIC team in designing such systems following a different approach is documented in a companion paper [17].

By comparing two variants of the 3-TeV collimation system, we have illustrated the difficult trade-off between system performance and length.

10 ACKNOWLEDGEMENTS

We thank O. Napoly of Saclay, and H.-J. Schreiber of DESY/Zeuthen for their collaboration and valuable help in developing various final-focus systems, assessing their performance, and estimating the background. We acknowledge early contributions by S. Fartoukh, J. Pancin, and E. Wildner fo the collimator and beam-dump design. We also express our thanks to G. Guignard for leading the CLIC design study, for his support and encouragement throughout this work, and for a careful reading of the manuscript, and to F. Ruggiero for organizing the CLIC activities in the SL/AP group.

11 REFERENCES

[1] F. Zimmermann, H. Burkhardt, T. Risselada, F. Schmidt, H.-J. Schreiber, "Final-Focus Schemes for CLIC at 3 TeV," Proc. 18th International Conference on High Energy Accelerators (HEACC2001), Tsukuba, Japan, CERN-SL-2001-010 AP and CLIC Note 476 (2001).

[2] M. Aleksa, R. Assmann, G.A. Blair, H. Burkhardt, A. Faus-Golfe, S. Redaelli, T. Risselada, S. Russenschuck, D. Schulte, F. Zimmermann, "Design Status of the CLIC Beam Delivery System," 8th EPAC, Paris, France, 3 - 7 Jun 2002, and CERN-SL-2002-031 (2002).

[3] R. Assmann, H. Burkhardt, S. Fartoukh, J.B. Jeanneret, J. Pancin, S. Redaelli, T. Risselada, F. Zimmermann, H.-J. Schreiber, "Overview of the CLIC Collimation Design," Proc. PAC'2001 Chicago, USA, CLIC Note 493, and CERN-SL-2001-036 (AP) (2001).

[4] F. Zimmermann, R. Assmann, G. Guignard, D. Schulte, O. Napoly, "Final-Focus System for CLIC at 3 TeV", Proc. EPAC 2000 Vienna, CERN-SL-2000-057 AP and CLIC Note 447 (2000).

[5] P. Raimondi and A. Seryi, "A Novel Final Focus Design for High Energy Colliders", PRL 86, 3779 (2001).

[6] P. Tenenbaum, et al., "Studies of beam optics and scattering in the Next Linear Collider post-linac collimation system," LINAC 2000, Monterey (2000).

[7] H. Grote and C. Iselin, "The MAD Program (methodical accelerator design) version 8.4: User's reference manual," CERN-SL-90-13-AP-REV.2 (1990).

[8] H. Grote, private communication (2001).

[9] F. Schmidt, E. Forest, E. McIntosh, "Introduction to the polymorphic tracking code : Fibre bundles, polymorphic Taylor types and "Exact tracking"', CERN-SL-2002-044-AP ; KEK-Report-2002-3 (2002).

[10] S. Redaelli, et al., "Comparison of Different Tracking Codes for Beam Delivery Systems of Linear Colliders," EPAC 2002 Paris, and CERN-SL-2002-033 (2002).

[11] D. Schulte, "Luminosity Limitations at the Multi-TeV Linear Collider Energy Frontier,", Proc. EPAC 2002, Paris (2002) p. 59

[12] E. d'Amico, G. Guignard, N. Leros, D. Schulte, "Simulation Package based on PLACET," PAC 2001 Chicago (2001) p. 3033

[13] D. Schulte, "Beam-Beam Simulations with GUINEA-PIG," ICAP98, Monterey, CA., USA, September 1998.

[14] R. Assmann et al., "CLIC Simulations from the Start of the Linac to the Interaction Point," EPAC 2002, Paris (2002).

[15] Y. Nosochkov, P. Raimondi, T.O. Raubenheimer, A. Seryi, "NLC Luminosity as a Function of Beam Parameters," Proc. EPAC 2002, Paris (2002) 479

[16] S. Redaelli, et al., "Simulation Tools for Luminosity Performance," these proceedings (2002).

[17] R. Assmann, H. Braun, H. Burkhardt, R. Corsini, S. Redaelli, D. Schulte, F. Zimmermann, A. Faus-Golfe, M. Velasco, "Beam-Dynamics Studies and Advanced Accelerator Research at CTF-3: Compact Final Focus, Laser Compton Scattering, Plasmas, etc.," these proceedings.

[18] M. Aleksa, et al., "The CLIC Study of Magnet Stability and Time-dependent Luminosity Performance," PAC2001, Chicago, CERN-SL-2001-036 AP, and CLIC Note 495.

[19] D. Schulte, "High Energy Beam-Beam Effects in CLIC," PAC 1999 New York (1999) p. 1668

[20] P. Chen and K. Yokoya, "Beam-Beam Phenomena in Linear Colliders," KEK Preprint 91-2 (1991).

[21] O. Napoly, "CLIC 3 TeV Interaction Region and Final Focus Studies," CERN-SL-99-054 AP, CLIC Note 414, DAPNIA/SEA-99-08 (1999).

[22] D. Schulte, F. Zimmermann, "The Crossing Angle in CLIC," Proc. PAC'2001 Chicago, USA, CERN/PS 2001-038 (AE), CLIC Note 484, and CERN-SL-2001-043 (AP) (2001).

[23] R. Assmann, H. Burkhardt, S. Fartoukh, J.B. Jeanneret, J.M. Jowett, F. Ruggiero, D. Schulte, A. Verdier, L. Vos, E. Wildner, F. Zimmermann, H. Owen, O. Napoly, "Design Studies of the CLIC 3-TeV Beam Delivery System and Damping Rings", Proc. EPAC 2000 Vienna, CERN-SL-2000-058 AP and CLIC Note 446 (2000).

[24] A.W. Chao, "Physics of Collective Beam Instabilities in High Energy Accelerators", Wiley (1993).

[25] M. Aleksa, S. Russenschuck, "Study of Some Options for the CLIC Final Focusing Quadrupole," CLIC Note 506 (2001).

[26] G. Guignard, private communication (2002).

[27] H. Burkhardt, Int. Workshop on Future e+e- Linear Colliders, Sitges 1999, CERN-SL-057-AP and CLIC Note 416.

[28] R. Assmann, et al., "Status of the CLIC Study on Magnet Stabilization and Time-Dependent Luminosity," EPAC 2002, Paris (2002).

[29] A. Drozhdin, et al., "Comparison of the TESLA, NLC and CLIC Beam Collimation Systems Performance," unpublished (2002).

[30] D. Schulte, F. Zimmermann, "Failure Modes in CLIC," Proc. PAC'2001 Chicago, USA, CLIC Note 492, and CERN-SL-2001-034 (AP) (2001).

[31] S. Fartoukh, et al., "Heat Deposition by Transient Beam Passage in Spoilers," CERN-SL-2001-012 AP (2001).

[32] J. Irwin in Chapter 9 of the "Zeroth-Order Design Report for the Next Linear Collider," The NLC Design Group, SLAC-Report-474 (1996).

[33] K. Yokoya, "Impedance Of Slowly Tapered Structures," CERN-SL/90-88 (AP) (1990).

[34] J.B. Jeanneret and E. Wildner, "Thermal and acoustic effects in CLIC beam absorbers," CERN-SL-99-072-AP.

[35] R. Pitthan and K. Thompson, private communications (1998).

[36] F. Zimmermann, NLC Acc. Phys. Note July 14 (1998).

[37] R. Brinkmann, P. Raimondi, A. Seryi "Halo Reduction by Means of Nonlinear Optical Elements in the NLC Final Focus System," PAC 2001, Chicago (2001).

[38] A. Faus-Golfe, F. Zimmermann, "A Nonlinear Collimation System for CLIC," 8th EPAC, Paris, France, 3 - 7 Jun 2002, and CERN-SL-2002-032 (2002).

[39] R. Helm, M. Lee, P. Morton, M.Sands, "Evaluation of Synchrotron Radiation Integrals," SLAC-PUB-1193 (1973).

[40] M. Sands, "The Physics of Electron Storage Rings," SLAC-121 (1970).

[41] G. Guignard (ed), "A 3 TeV Linear Collider Based on CLIC Technology," CERN 2000-008.

[42] G.A. Blair, "Simulations of the CLIC Beam Delivery System using BDSIM," CLIC Note 509 (2002).

[43] V. Bargmann, L. Michel, and V.L. Telegdi, "Precession of the Polarization of Particles Moving in a Homogeneous Electromagnetic Field". Phys. Rev. Lett. 2 (1959) 435.

[44] R. Assmann and F. Zimmermann, "Polarization Issues at CLIC," submitted to Proc. Snowmass 2001, CERN SL-2001-064 (AP) and CLIC Note 501 (2001).

[45] D. Schulte, private communication (1999).